$RE_3Mo_{14}O_{30}$ and $RE_2Mo_9O_{19}$, two reduced rare-earth molybdates with honeycomb-related structures (*RE* = La - Pr)

Scott Forbes, Tai Kong, and R.J. Cava*

Department of Chemistry Princeton University Princeton NJ 08544 USA

Abstract

The previously unreported $RE_3Mo_{14}O_{30}$ and $RE_2Mo_9O_{19}$ phases were synthesized in vacuo from rare-earth oxides, molybdenum oxide, and molybdenum metal using halide fluxes at 875-1000°C. Both phases adopt structures in the triclinic $P\bar{1}$ space group albeit with several notable differences. The structures display an ordering of layers along the *a*-direction of the unit cell, forming distinct honeycomb-related lattice arrangements composed of MoO_6 octahedra and vacancies. Mo-Mo bonding and clusters are present - the $RE_3Mo_{14}O_{30}$ structure contains Mo dimers and rhomboid tetramers, while the $RE_2Mo_9O_{19}$ structure contains rhomboid tetramers and an unusual arrangement of planar tetramers, pentamers, and hexamers. Magnetic measurements found the $RE_2Mo_9O_{19}$ phases to be simple paramagnets, while $La_3Mo_{14}O_{30}$ was observed to order antiferromagnetically at 18 K. Electrical resistivity measurements confirmed all samples to behave as nondegenerate semiconductors.

Keywords: rare-earth molybdates; crystal structure; magnetic properties; electrical resistivity.

* Corresponding author

Introduction

Solid state materials containing reduced molybdenum make a diverse and complex class of structures owing to the extraordinary ability of molybdenum to form a variety of different cluster and metal-metal bonding geometries. Many such compounds have been studied for their unusual electronic properties, particularly with regards to superconductivity[1]. The most common types of molybdenum clusters include Mo_2 dimers, Mo_3 triangles, Mo_4 tetrahedra, and Mo_6 octahedra. Extended variations of the aforementioned groups are also observed and are based on the capping of edges and faces of Mo_6 octahedra. Octahedral Mo_6 *trans*-face-capping is common for larger anion ligands, most notably sulfur, selenium, and tellurium. This type of connectivity yields clusters with general formula Mo_{3n+3}, ranging from groups as small as n = 2, such as the Mo_9 groups in $Ag_xCsMo_9O_{11}$ and $Ag_xClMo_9O_{11}$[2], to infinitely long n = ∞ $[Mo_3]_\infty$ chains, as is the case for $AgMo_6Te_6$[3] and related phases. Face-capping of Mo_6 octahedra also forms the basis for an expansive series of $M_xMo_6X_8$ phases (M = a cation, X = S, Se, Te), the so-called Chevrel phases, which includes over 100 compounds. The cluster formations of these Mo atoms is also responsible for good superconducting behavior in some members of the series[4,5], most notably $PbMo_6S_8$, which has a critical temperature to the superconducting state of 15 K[6]. Cis-face-capping of Mo_6 octahedra is rare by comparison, but has been observed previously in the $LaMo_8O_{14}$ structure[7]. By contrast, stacking of *trans*-edge-sharing octahedral units can be seen for molybdenum oxides, yielding linear chain units with a general formula of Mo_{4n+2}. As was the case for face-capping, an extensive series of phases may be produced by extension of the cluster unit. This has been observed for Mo_2O_{10} clusters in many phases such as $La_4Mo_2O_{11}$[8], and may also be extended to infinite chains, as observed in $NaMo_4O_6$[9]. Further structural modifications have been observed in cases of mono- and bi-capped edge-sharing clusters[10], alternating trans-edge-sharing chain sequences[11], and edge-sharing between three Mo_6 octahedral groups[12]. Thus, ternary and quaternary molybdenum-based phases are an attractive field of study both in a structural sense and in the search for materials with desirable physical properties. As such, it is of interest to investigate structures with other possible conformations of molybdenum atoms to further expand the range of these materials.

Honeycomb-type structures form an interesting class of materials that has also been studied in detail. These structures are composed of hexagonal arrangements of atoms in either mono- or bi-layers, and as a result of their reduced dimensionalities, have been shown to yield interesting electrical and thermal properties, most notably in graphene[13–15], as well as in other materials

including $RuCl_3$[16] and group-III nitrides[17,18]. Ternary and quaternary solid state materials containing magnetically active elements and honeycomb-type lattices are common, with materials such as $BaCo_2P_2O_8$[19] and $Mn_2V_2O_7$[20] being good examples of magnetically frustrated species. Aside from magnetism, honeycomb-type structures have been shown to yield other noteworthy physical properties, including ionic conductivity[21] and thermoelectricity[22]. Structures including this lattice arrangement are generally limited to materials containing first row transition metals or main group elements. Studies involving the heavier transition metals are less common, but have nevertheless yielded similar attractive physical properties, such as the metal-insulator transition in Li_2RuO_3[23], topological electronic states in LiAuSe and KHgSb[24], and superconductivity in lithium-intercalated β-ZrNCl[25]. With this in consideration, there is a great deal of potential to find interesting properties in novel honeycomb-type lattice structures containing second- and third-row transition metals if such structures can be made.

Here we report our experiments involving the *RE*-Mo-O system, which have led to finding two previously unreported phases that both contain a modification of a honeycomb-type lattice in their crystal structures and may form the basis for a new family of reduced ternary molybdates. We report the existence of two novel rare-earth molybdate phases, $RE_3Mo_{14}O_{30}$ and $RE_2Mo_9O_{19}$ (*RE* = La – Pr). The conditions of formation, crystal structures, and physical properties of each phase are presented and discussed.

Experimental

Synthesis. $La_3Mo_{14}O_{30}$, $La_2Mo_9O_{19}$, and $Ce_2Mo_9O_{19}$ samples were made using high-purity molybdenum (99.9 wt.%, Alfa Aesar), MoO_3 (99.9 wt.% Alfa Aesar), La_2O_3 (99.99 wt.% Strem Chemicals), CeO_2 (99.5 wt.% Johnson-Mathey Inc.), and Pr_6O_{11} (99.9 wt.% Johnson-Mathey Inc.). The synthetic methods employed required metal halide fluxes including KI (99.9 wt.% J. T. Baker Chemical co.), RbI (99.8 wt.% Alfa Aesar), NaI (99.5 wt.% EMD Chemicals Inc.), and $BaBr_2$ (99.3 wt.% Alfa Aesar). Samples were prepared by mixing specific amounts of rare-earth oxide, MoO_3, and Mo metal with a 1.6:1 mass ratio of flux to sample. The constituents were mixed and added to alumina crucibles which were then sealed under vacuum in 10-15 cm quartz glass tubes lined with alumina wool at the base to avoid tube cracking from thermal expansion. Samples were then heated in box furnaces at 900°C for 72 hours to achieve the best purities.

The $RE_3Mo_{14}O_{30}$ and $RE_2Mo_9O_{19}$ phases can be prepared using salt fluxes at temperatures of 875°C-1000°C, although 900°C was found to produce the best results. Variations in

temperature, time, and loading composition primarily result in the formation of MoO_2 as an impurity. Furthermore, only NaI, KI, RbI, CsI, $SrBr_2$, and $BaBr_2$ were determined to yield the desired phases, with other flux agents or a lack thereof generating other products. Upon reaction completion, all samples were washed with dilute hydrochloric acid to dissolve unwanted impurities. After about 10 minutes, samples were then flushed with water and vacuum filtered using a fritted funnel to remove any residual salt. Samples were then washed and filtered with ethanol to remove traces of iodine (from thermal decomposition) and achieve dryness. Pure samples of $La_3Mo_{14}O_{30}$, $La_2Mo_9O_{19}$, and $Ce_2Mo_9O_{19}$ appear as a shiny, black powder. All purified materials remain stable in vacuo up until about 800°C, above which gradual decomposition into MoO_2 and other impurities is observed. All samples were observed to remain stable in laboratory air at room temperature for at least several months.

X-ray Single Diffraction. Single crystals of $La_3Mo_{14}O_{30}$, $La_2Mo_9O_{19}$, and $Ce_2Mo_9O_{19}$ were analyzed on a Bruker SMART APEX Duo diffractometer equipped with a CCD detector. All crystals studied were obtained from samples which used $BaBr_2$ as the flux agent, as it was determined to yield the largest and highest quality crystals. All data collection was performed using Mo K_α radiation and at room temperature. Intensity corrections for Lorentz and polarization effects were performed with the SAINT program[26]. The unit cell determination and subsequent data collection, integration, and refinement were all performed using the Bruker APEX II software package. Crystal structures were determined using the SHELX software[27].

X-ray Powder Diffraction. Each sample was analyzed by X-ray powder diffraction on a Bruker D8 ADVANCE Eco instrument using Cu Kα incident radiation. Approximately 50 mg of sample was ground up using a mortar and pestle and deposited on a micro cover glass which was then mounted on a sample puck. The data was collected in the 2θ range between 10° and 70° and analyzed using the Rietveld refinement method (Rietica program[28]) to determine sample purity and lattice constants. The structural parameters obtained from the X-ray single crystal data were used as the initial models for refinements. Sufficiently pure samples were then selected for physical properties measurement based on X-ray powder refinement results.

Magnetic Measurements. Bulk samples of $La_3Mo_{14}O_{30}$, $La_4Mo_{18}O_{38}$, and $Ce_4Mo_{18}O_{38}$ were analyzed for their temperature dependent magnetic behavior. Approximately 40 mg of each sample was packed in plastic samples holders and analyzed for magnetism using a Quantum Design (QD) Physical Property Measurement System (PPMS) equipped with a vibrating sample

magnetometer. A magnetic field strength of 20 Oe was used to test for superconductivity in the 1.8-12 K temperature range, while a 30 kOe field strength was used to characterize sample magnetism in the 2-300 K temperature range. The data sets were fitted to the generalized Curie-Weiss equation to obtain the Weiss temperature (θ) and effective magnetic moments (μ_{eff}).

$$\chi = \chi_0 + \frac{C}{T-\theta} \quad (1)$$

Electrical Resistivity Measurements. Pure samples of $La_3Mo_{14}O_{30}$, $La_2Mo_9O_{19}$, and $Ce_2Mo_9O_{19}$ were pressed as ¼ inch diameter pellets, sealed in evacuated quartz glass tubes, and annealed at 800°C for 72 hours to ensure rigidity. Powder X-ray diffraction analysis confirmed no decomposition or generation of impurities by this method. After annealing, samples were then cut into rectangular bars with dimensions of approximately 2 x 2 x 3 mm using a diamond-coated wheel saw and water as a lubricant to avoid oxidation due to friction. Four-probe DC electrical resistivity measurements were performed using a QD PPMS. Platinum wire leads were attached on each sample using DuPont 4922N silver paint.

Results and Discussion

Formation of $RE_3Mo_{14}O_{30}$ and $RE_2Mo_9O_{19}$. Samples of $RE_3Mo_{14}O_{30}$ and $RE_2Mo_9O_{19}$ may be prepared via salt flux reactions at temperatures of 875-1000°C (*RE* = La – Pr). Our experiments determined that KI as the flux agent gave the best results, and as such, it was used to obtain pure phases. Samples with *RE* = La could be prepared at high purity for either phase, while samples for *RE* = Ce could only reliably be made pure for $Ce_2Mo_9O_{19}$. Our attempts to extend the rare-earth series further demonstrated that samples with *RE* = Pr could only be formed in low amounts, and neither phase could be synthesized for heavier *RE*. It is worth mentioning that our loading compositions to yield Ce- and Pr-containing $RE_3Mo_{14}O_{30}$ and/or $RE_2Mo_9O_{19}$ phases included CeO_2 and Pr_6O_{11}, which contain some or all of their *RE* atoms in the 4+ oxidation state. However, we conclude that the cerium and praseodymium in our samples are exclusively trivalent, since they are isostructural with the corresponding $La_3Mo_{14}O_{30}$ and $La_2Mo_9O_{19}$ phases, and the smaller[29], tetravalent Ce^{4+} and Pr^{4+} would likely not be found in the large coordination polyhedra for the *RE* atoms in these structures. Furthermore, the bond valence sum (BVS) model using the method outlined by Brese and O'Keeffe[30] determines the valence of Ce atoms in $Ce_2Mo_9O_{19}$ to be 2.98 based on our X-ray single crystal data if the bond length parameters for Ce^{3+} are assumed in the calculations (compared to the implausible valence of 2.14 if the Ce^{4+} parameters are assumed).

Finally, the reducing conditions of the synthesis do not favor the presence of rare earth ions in high oxidation states - we conclude that reduction of the CeO_2 and Pr_6O_{11} starting materials performed by elemental molybdenum in situ.

Iodide salt fluxes, particularly KI, yielded the purest products, while the bromide salt fluxes $SrBr_2$ and $BaBr_2$ yielded better and larger (although in the 10s of microns size range) crystals. Pure samples of all phases assume the form of a black, shiny, crystalline powder, their color likely indicating semiconducting behavior. Interestingly, using a stoichiometric loading composition for either phase results in large amounts of a MoO_2 impurity, typically about 20-30% weight percentage. Additionally, given the similar compositions for $RE_3Mo_{14}O_{30}$ and $RE_2Mo_9O_{19}$ (which can also be written as $RE_3Mo_{13.5}O_{28.5}$), it is difficult to devise a synthetic pathway which will yield a single phase and not a mixture of the two. As such, the loading compositions must be carefully tuned to yield the desired products in high purity. Our experiments determined a satisfactory synthetic route for the formation of $La_3Mo_{14}O_{30}$, $La_2Mo_9O_{19}$, and $Ce_2Mo_9O_{19}$, and is presented in the Supporting Information.

In each case where a pure product could be obtained, it was observed that the loading composition incorporated a larger amount of elemental molybdenum and a smaller amount of molybdenum oxide than expected (in other words the average Mo valence in the starting material is less than in the products) This can be explained by the need for reduction - the formation of MoO_2 is seen in a stoichiometric loading composition, with compositions using more metal resulting in a more strongly reducing chemical environment. Indeed, both $RE_3Mo_{14}O_{30}$ and $RE_2Mo_9O_{19}$ contain molybdenum which is more reduced than in MoO_2 (average Mo oxidation state for $RE_3Mo_{14}O_{30} \approx 3.64+$, $RE_2Mo_9O_{19} \approx 3.56+$). Loading compositions that used even more reducing conditions generally resulted in the formation of $REMo_8O_{14}$ (average Mo oxidation state ~ 3.1+). Lastly, it is worth mentioning that these phases are most likely restricted for *RE* = La-Pr, which are the largest members of the rare-earth series in terms of atomic radius[29]. We speculate that this is due to the fact that the crystal structures of $RE_3Mo_{14}O_{30}$ and $RE_2Mo_9O_{19}$ contain very large sites occupied by rare-earth atoms that cannot support the bonding requirements for later members of the rare-earth series due to their smaller atomic radii. This is corroborated by the fact that $RE_3Mo_{14}O_{30}$ contains 10-coordinate rare-earth sites and can only be made for La in high purity, while $RE_2Mo_9O_{19}$, which contains 11-coordinate rare-earth sites, can be made pure only for either La or Ce. Samples containing Pr could only yield $Pr_2Mo_9O_{19}$, and only in small amounts. No

successful experiments occurred for the heavier members of the rare-earth series for $RE_3Mo_{14}O_{30}$ or $RE_2Mo_9O_{19}$ regardless of reaction conditions.

Structure Refinements A summary of the refinement results is presented in Tables 2 and 3. The $RE_3Mo_{14}O_{30}$ and $RE_2Mo_9O_{19}$ phases both crystallize in the triclinic $P\bar{1}$ space group. The initial structural model for the $RE_2Mo_9O_{19}$ phases placed the Mo3 atoms on a 1*f* site, but a significant improvement in the model was observed when these atoms were split into the surrounding 2*i* site and allowed to refine in atomic coordinates at a fixed 50% occupancy (the split sites are too close together to be occupied simultaneously). The resulting model achieved substantially improved $U_{22}/U_{33}/U_{eq}$ parameters and crystallographic R-factors. We considered the possibility of a supercell that would allow for an ordering of the Mo3 atoms, but we did not find evidence for supercell peaks in either the X-ray single crystal or powder diffraction data. Further information on the crystal structures, including positional and thermal displacement parameters and bond lengths can be found in the Supporting Information and may be obtained from the Fachinformationszentrum Karlsruhe, 76344 Eggenstein-Leopoldshafen, Germany (fax (49) 7247-808-666; email crysdata@fiz.karlsruhe.de), by quoting the CSD depository numbers 433469-433471.

Structural Features of $RE_3Mo_{14}O_{30}$. Our discussion of the $RE_3Mo_{14}O_{30}$ structure is limited to the $La_3Mo_{14}O_{30}$ phase, as we could not obtain crystals for other *RE*. The $RE_3Mo_{14}O_{30}$ phase adopts the $P\bar{1}$ space group and is primarily composed of a network of MoO_6 octahedra, with two different types of REO_{10} polyhedra interwoven into the structure. The contents of the unit cell are arranged such that distinct layers are stacked along the *a*-direction, the layers alternating between an exclusive MoO_6 octahedral framework and mixed interlayers consisting of MoO_6 octahedra and REO_{10} polyhedra (Figure 1). The $[RE1]O_{10}$ polyhedra (*RE*-O distances of 2.43(1) - 2.94(4) Å) can be described as tricapped, defect rectangular prisms, where one of the eight corners of the prism is absent due to a *RE*1-O2 separation of > 3 Å. The *RE* atoms are notably displaced from the centers of each polyhedron as a means to increase their separation (*RE*-*RE* distance of 3.73(4) Å). Such a large difference in *RE*-O bond distances, including the long contacts of ~ 2.9 Å, is not unheard of, and is comparable to what is found for the La atoms in $La_4Mo_2O_{11}$[8]. Similarly, the $[RE2]O_{10}$ polyhedra (*RE*-O distances of 2.55(3) - 2.70(2) Å) assume the form of a tetracapped, defect rectangular prism, where two of the eight corners of the prism are absent due to a *RE*2-O4

separation of > 3 Å. Together, the two different types of REO$_{10}$ polyhedra are connected to each other in infinite chains via edge-sharing, creating a RE_3O$_{26}$ unit.

The gaps between the chains are filled by MoO$_6$ octahedra that are connected to each other by both corner- and edge-sharing. These form chains along the same direction as is found for the rare earth chains (Figure 2). The Mo atoms in these chains are close enough to indicate the formation of bonds (Mo-Mo distances of 2.58(3) - 2.63(2) Å), yielding a set of Mo$_2$ dimers and rhomboid Mo$_4$ tetramers that alternate in sequence. Including the associated oxygens, the dimers and tetramers can be viewed as Mo$_2$O$_{10}$ and Mo$_4$O$_{16}$ clusters, respectively. The dimers and tetramers are both positioned on inversion centers, with the tetramers located at a 1*a* site at the corners of the unit cell and the dimers located at a 1*g* site on unit cell faces.

One of the more interesting structural features of RE_3Mo$_{14}$O$_{30}$ is derived from the layers that contain exclusively MoO$_6$ octahedra, which are situated between the layers described above. The MoO$_6$ octahedra in these layers are connected to one another by edge-sharing, resulting in the formation of two types of Mo$_4$O$_{16}$ clusters that contain rhomboid Mo$_4$ tetramers (Mo-Mo distances of 2.53(3) - 2.67(4) Å), similar to those observed in K$_2$Mo$_8$O$_{16}$[31]. These tetramers are situated around the 1*e* and 1*f* site inversion centers located at faces of the unit cell. More importantly, the MoO$_6$ octahedra in this layer form a defect honeycomb-type lattice defined by Mo-Mo bonds and vacancies. In a standard honeycomb lattice, the atoms at the centers of the octahedra are all bonded together in a hexagonal formation. Subtle differences may arise due to the difference chemistry of a second "spacer" metal atom, such as the tetrahedrally coordinated zinc in Zn$_3$Mo$_3$O$_8$[32], or due to lattice shearing in the high pressure MnPS$_3$ and MnPSe$_3$ phases[33]. However, in RE_3Mo$_{14}$O$_{30}$, several of the potential "spacer atom" positions do not contain any atoms and can be considered as vacancies. This in turn perturbs the ideal metal-metal bonding network. Due to the vacancies, this lattice can instead be described as being composed of chains of four MoO$_6$ octahedra that are connected to form a Mo$_4$O$_{18}$ unit. These individual chain units are separated from one another along the stacking direction by vacancies, which alternate in a single-double pattern (Figure 3). This arrangement is different in the RE_2Mo$_9$O$_{19}$ phases which shall be discussed below.

If we consider the stoichiometric formula of RE_3Mo$_{14}$O$_{30}$ by simple electron counting rules, there would be (30 x 2) – (3 x 3) = 51 electrons required from molybdenum atoms to achieve charge neutrality. Obviously, there is no easy way to attain integer formal charges on every Mo atom this way in RE_3Mo$_{14}$O$_{30}$, and thus the implied bonding in this structure is quite complex. In

order to obtain further insight on the bonding nature of the $RE_3Mo_{14}O_{30}$ phase, the oxidation states of each of the Mo atoms were determined using the method described by Brown and Wu[34] to calculate the bond strength *s* for Mo-O bonds using equation 2. A summary of the calculated values for each Mo atom for the $La_3Mo_{14}O_{30}$ structure is presented in the Supporting Information. Via these calculations, we obtain a value of 51.13(9) as a total charge for all Mo atoms in the structure, which agrees well with the expected value for a charge balanced structure. Each tetramer can be described as a group containing two types of Mo atoms which bond to two or three other Mo atoms. The Mo atoms with three Mo-Mo bonds are all calculated to have lower oxidation states than those with only two bonds, which is to be expected considering their more reduced environments. It follows then that the Mo atoms in the tetramer units are noticeably more reduced than the Mo atoms in the dimer units.

$$s(\mathrm{Mo}-\mathrm{O}) = \left[\frac{d(\mathrm{Mo}-\mathrm{O})}{1.882}\right]^{-6} \qquad (2)$$

The Mo_4 tetramers in $RE_3Mo_{14}O_{30}$ are very similar to those observed in $K_2Mo_8O_{16}$[31], except that all of the Mo-Mo distances are about 2.60 - 2.65 Å, which are typical of Mo-Mo single bonds. If that is the case, then there exist five bonding orbitals for the Mo_4 tetramer units, for which we can assign ten electrons each, resulting in three electrons left over to be assigned in order to meet the 51 electron count required for a charge balanced structure. Thus, the remaining three electrons can be assigned to the Mo_2 dimers, yielding a bond order of 1.5 and one unpaired electron. A detailed list of all Mo-Mo distances in $RE_3Mo_{14}O_{30}$ is provided in the Supporting Information.

Structural Features of $RE_2Mo_9O_{19}$. The $RE_2Mo_9O_{19}$ phase also adopts the $P\bar{1}$ space group, sharing many similarities with the $RE_3Mo_{14}O_{30}$ structure, but also showing some key differences. Much like $RE_3Mo_{14}O_{30}$, the $RE_2Mo_9O_{19}$ structure is divided into alternating layers along the *a*-direction of its unit cell, with one layer consisting of exclusively MoO_6 octahedra, and another layer that contains MoO_6 octahedra and REO_{11} polyhedra (Figure 4). The REO_{11} polyhedra are quite similar to the $[RE1]O_{10}$ polyhedra seen in $RE_3Mo_{14}O_{30}$, and can also be described as tricapped rectangular prisms, except that none of the corners of the prism are missing (*RE*-O distances of 2.40(3) – 2.92(3) Å). As a result, these *RE*-O polyhedra are connected to each other by an alternating arrangement of edge- and four vertex face-sharing, forming a RE_2O_{18} unit, and

extend throughout the structure as an infinite chain. The *RE* atoms are also displaced from the centers of each polyhedron as a means to reduce cation-cation repulsion (*RE*-*RE* distances are 3.63(3) Å for $La_2Mo_9O_{19}$, and 3.65(3) Å for $Ce_2Mo_9O_{19}$). MoO_6 octahedra occupy the gaps between the chains, and are connected to one another by corner- and edge-sharing, forming a concurrent set of chains interwoven with the REO_{11} polyhedral chains (Figure 5). Unlike $RE_3Mo_{14}O_{30}$, however, these chains do not form dimers, and instead form Mo_4 rhomboid tetramers and Mo_4O_{16} clusters exclusively (Mo-Mo distances of 2.59(2) - 2.63(3) Å). The tetramers formed by these chains are positioned on the 1*c* site inversion centers located at the edges of the unit cell.

One noteworthy feature unique to $RE_2Mo_9O_{19}$ is the presence of a disordered Mo atom in its crystal structure. Our initial refinements placed the Mo3 atoms on a 1*f* crystallographic site, as described above, but this was observed to yield unusually high temperature factors (U_{eq} = 0.0206(2) compared to the average U_{eq} = 0.00508(7) for the other Mo atoms). The resulting crystal solution would give decent R-factors, but would leave Mo3 atoms unable to participate in Mo-Mo bonding due to large interatomic separations (Mo-Mo distances of 2.75(2) – 2.82(3) Å). A separate model was then constructed, where Mo3 atoms were positioned ~0.2 Å off the 1*f* site and allowed to refine to a general 2*i* position, but with its occupancy fixed at 50% (the displaced sites are too close together to be simultaneously occupied), yielding a set of long and short Mo-Mo contacts (2.57(3) – 2.67(3) Å vs. 2.94(2) – 2.97(3) Å in $Ce_2Mo_9O_{19}$. This new structural model resulted in a substantial improvement in temperature factors and a significant reduction in the crystallographic R-factor (see Tables 1 and 2), yielding a better model at the 0.995 confidence level[35]. The improved model assumes a random arrangement of Mo3 atoms around the 1*f* inversion center, but forbids the possibility of two atoms overlapping. The resulting solution allows for the formation of planar Mo_4 tetramers, Mo_5 pentamers, and Mo_6 hexamers (Mo-Mo distances of 2.57(2) - 2.67(3) Å), yielding Mo_4O_{16}, Mo_5O_{19}, and Mo_6O_{22} clusters, respectively. However, since the locations of Mo3 atoms are random, these groups have a random order in the crystal structure (Figure 6). The resulting conformation of Mo-Mo bonding resembles the infinite triangular chains observed in the Hollandite-type $NdMo_6O_{12}$ phase[36], although the long contacts created by Mo3 displacement prevents this type of bonding. A summary of the Mo-Mo contacts with respect to these two models is presented in the Supporting Information.

As is the case with $RE_3Mo_{14}O_{30}$, the $RE_2Mo_9O_{19}$ phases also form a honeycomb-derived layered substructure between the layers that contain the *RE*-O polyhedral chains. These layers

contain MoO_6 exclusively, and are stitched together by corner- and edge-sharing. The resulting arrangement of octahedra yields planar tetramers, pentamers, and hexamers composed of Mo atoms. As noted above, due to the displacements of the Mo3 atoms from the 1*f* inversion center, the exact order of these groups is random in the structure. As was the case with $RE_3Mo_{14}O_{30}$, an ordering of vacancies perturbs the ideal metal-metal bonding framework that would be present for a traditional honeycomb lattice. Similarly, there is a distinct MoO_6 octahedral chain which defines this framework, except in $RE_2Mo_9O_{19}$, this chain is composed of five MoO_6 octahedra instead of four (as found in $RE_3Mo_{14}O_{30}$), yielding Mo_5O_{22} units which are separated from each other along the stacking direction by two vacancies each time instead of an alternating arrangement of one and two vacancies (Figure 3 above). A summary of structural differences between $RE_3Mo_{14}O_{30}$ and $RE_2Mo_9O_{19}$ is presented in the Supporting Information.

If we use simple electron counting rules, there would be (19 x 2) – (2 x 3) = 32 electrons required from molybdenum atoms to achieve neutrality in this structure. As for $La_3Mo_{14}O_{30}$, we can calculate the formal oxidation numbers of each of the Mo atoms in the $RE_2Mo_9O_{19}$ structures using equation 2 (see Supporting Information). Similar to $RE_3Mo_{14}O_{30}$, an obvious trend is seen for which Mo atoms with more Mo-Mo bonds have lower oxidation states and vice versa, although an exception is noted for the disordered Mo3 atoms, which have higher oxidation states despite being bonded to more Mo atoms on average. Our calculations for the sum of the oxidation states of all Mo atoms in each structure yield a value of 32.31(9) for $La_2Mo_9O_{19}$ and 32.53(9) for $Ce_2Mo_9O_{19}$, which also agree with the expected value for charge neutrality.

Considering that the Mo_4 tetramers in $RE_2Mo_9O_{19}$ are very similar to those observed in $RE_3Mo_{14}O_{30}$, we can also assume that ten electrons are present in each unit. If that is the case, then there are 12 electrons left to be distributed into the disordered Mo-Mo bonding network. To better rationalize the bonding character, we can say that the Mo groups in the honeycomb layer can be simplified as an average Mo_5O_{22} cluster with five Mo-Mo bonds. If we assume that each of the bonds in these units are two-electron bonds, then there are still two electrons remaining. Clearly, the Mo-Mo bonding character in $RE_2Mo_9O_{19}$ is far more complicated for $RE_2Mo_9O_{19}$ than in $RE_3Mo_{14}O_{30}$ as a result of the coexistence of tetramers, pentamers, and hexamers in the honeycomb layer. Since none of the Mo-Mo distances in this layer are short enough to justify double bonds, we suggest that the remaining two electrons may occupy non-bonding portions of the d-orbitals in these units, as is the case for $K_2Mo_8O_{16}$[31].

Magnetic behavior of $RE_3Mo_{14}O_{30}$ and $RE_2Mo_9O_{19}$. The temperature-dependent magnetization data for $La_2Mo_9O_{19}$ and $Ce_2Mo_9O_{19}$ show a paramagnetic behavior down to 2 K. No signature in magnetization can be associated with a long-range magnetic ordering (Figure 7). By contrast, $La_3Mo_{14}O_{30}$ displays a sharp decrease in magnetization at about 18 K, which may come from an antiferromagnetic transition. At the lowest temperatures studied, there is an upturn in magnetization, possibly due to the presence of a small fraction of magnetic impurities. No superconducting behavior was observed in any of the three compounds down to 2 K. The characteristic magnetic parameters obtained from fitting Equation 1 to magnetization data (50-300 K) are summarized in Table 3. The difference in magnetism between $La_3Mo_{14}O_{30}$ and $La_2Mo_9O_{19}$ may be due to their differences in Mo-Mo bonding, most notably the unpaired electron presumed to be in the Mo-Mo dimer unit in $La_3Mo_{14}O_{30}$. Future studies into the local magnetic moments within each structure may be needed to better determine their respective origins of magnetism.

In the cases of $La_3Mo_{14}O_{30}$ and $La_2Mo_9O_{19}$, we can assume that the magnetism originates entirely from the molybdenum atoms, due to the lack of *f*-electrons on lanthanum. As such, we can calculate the effective magnetic moment per Mo atom in each structure. Assuming all Mo atoms contribute equally to the magnetization, the effective moment per Mo are 0.6 μ_B for $La_3Mo_{14}O_{30}$ and 0.2 μ_B for $La_2Mo_9O_{19}$. Magnetic ordering is known to be uncommon for 4d metals due to the dispersive nature of their *d*-orbitals, but is not unheard of in rare earth molybdates, such as the metamagnetic transition observed in $La_5Mo_4O_{16}$[37]. For $Ce_2Mo_9O_{19}$, there is one *f*-electron in each Ce^{3+} which is also able to contribute to the magnetic behavior of the sample. This is manifested in both the significantly higher magnetic moment at lower temperatures and in the experimentally determined effective magnetic moment μ_{eff}. A value of $\mu_{eff} = 3.3\ \mu_B$ for the $Ce_2Mo_9O_{19}$ sample was obtained. Assuming that the Mo atoms in $Ce_2Mo_9O_{19}$ contribute equally to the magnetic response as compared to $La_2Mo_9O_{19}$, the effective moment of Ce in $Ce_2Mo_9O_{19}$ is estimated to be 2.3 μ_B. This value is close to the theoretical value for Ce^{3+} (2.5 μ_B)[38]. Both $La_3Mo_{14}O_{30}$ and $Ce_2Mo_9O_{19}$ deviate from the Curie-Weiss behavior at low temperatures. These behaviors are attributed to the antiferromagnetic transition in $La_3Mo_{14}O_{30}$ and the ground state splitting of cerium atoms at low temperature for $Ce_2Mo_9O_{19}$[39].

Electrical resistivity behavior of $RE_3Mo_{14}O_{30}$ and $RE_2Mo_9O_{19}$. The measured electrical resistivity data for all $RE_3Mo_{14}O_{30}$ and $RE_2Mo_9O_{19}$ samples reveals an exponential decrease with increasing temperature (Figure 8). High electrical resistances for all samples rendered us unable

to measure data for temperatures below ~ 40 K. The data is consistent with behavior of nondegenerate semiconductors, as expected from the black pigmentations, and in agreement with our analysis of the crystallographic data indicating charge balanced structures. Owing to their similar structures, the $La_2Mo_9O_{19}$ and $Ce_2Mo_9O_{19}$ samples share similar electrical resistivities throughout the entire measured temperature range. The $La_3Mo_{14}O_{30}$ sample displays similar behavior to the $RE_2Mo_9O_{19}$ samples, but is a bit less resistive. The activation energies for all samples were calculated based on the Arrhenius equation and were all determined to be ~0.10-0.15 eV, which are typical values for narrow band gap semiconductor (Table 3).

Conclusions

We have found and successfully obtained pure products of two previously unreported rare-earth molybdates $RE_3Mo_{14}O_{30}$ and $RE_2Mo_9O_{19}$ for *RE* = La – Pr. The crystal structures of these compounds display share many similarities to one another, including *RE*-O polyhedral chains, a distinct honeycomb-type layer, and several types of Mo-Mo bonding interactions in their respective crystal structures. The $RE_2Mo_9O_{19}$ phase in particular contains a unique arrangement of planar tetramers, pentamers, and hexamers owing to the disordered nature of its crystal structure. Considering the common structural features between $RE_3Mo_{14}O_{30}$ and $RE_2Mo_9O_{19}$, we propose that other currently unreported structures may be found by a modified synthetic approach.

Magnetic measurements confirmed that $RE_2Mo_9O_{19}$ phases do not display any form of long range ordering, but that $La_3Mo_{14}O_{30}$ does display what appears to be antiferromagnetic ordering at 18 K. In the case of the La-containing samples, it is assumed that the weak magnetic behavior originates from the Mo atoms, while the magnetization of $Ce_2Mo_9O_{19}$ is dominated by the *f*-electron on the cerium atoms. Electrical resistivity measurements confirmed both $RE_3Mo_{14}O_{30}$ and $RE_2Mo_9O_{19}$ to be narrow band gap semiconductors with electronic band gaps of about 0.10-0.15 eV, which is consistent with their black pigmentations and the Mo oxidation state calculations based on the crystal structures. Due to the low dimensionality and the honeycomb layers, it may be worthwhile to investigate the role of structural perturbation by intercalation and atomic substitution on the physical properties in these structures.

Acknowledgements

This work was supported by the US Department of Energy, Division of Basic Energy Sciences, grant number DE-FG02-98ER45706.

Supporting Information. A summary of atomic parameters, bond distances, and Mo-Mo bonding arrangements for the $RE_3Mo_{14}O_{30}$ and $RE_2Mo_9O_{19}$ X-ray single crystal solutions is presented. These data are free of charge and can be found at http://pubs.acs.org.

Table 1. Crystallographic and refinement data for the $RE_3Mo_{14}O_{30}$ and $RE_2Mo_9O_{19}$ crystals.

	$La_3Mo_{14}O_{30}$	$La_2Mo_9O_{19}$	$Ce_2Mo_9O_{19}$
Refined composition	$La_3Mo_{14}O_{30}$	$La_2Mo_9O_{19}$	$Ce_2Mo_9O_{19}$
Space group	$P\,\bar{1}$	$P\,\bar{1}$	$P\,\bar{1}$
Radiation	Mo K_α (0.71073 nm)		
Scan mode	Omega and Phi		
Temperature	293 K		
Crystal dimensions (mm)	0.070 x 0.060 x 0.060	0.080 x 0.070 x 0.050	0.060 x 0.060 x 0.050
***a* (Å)**	7.058(1)	7.092(1)	7.081(1)
***b* (Å)**	7.531(2)	7.410(2)	7.402(2)
***c* (Å)**	10.155(2)	7.429(2)	7.423(2)
α	95.12(3)	61.08(3)	60.99(3)
β	99.91(3)	83.23(3)	83.30(3)
γ	97.89(3)	77.54(3)	77.62(3)
Volume (Å^3)	523.1(2)	333.7(1)	332.3(1)
p_{calc} (g/cm^3)	7.110	7.192	7.235
Z	1	1	1
Index ranges	$-14 \le h \le 14$ $-15 \le k \le 15$ $-20 \le l \le 20$	$-14 \le h \le 14$ $-14 \le k \le 14$ $-14 \le l \le 14$	$-14 \le h \le 13$ $-14 \le k \le 14$ $-14 \le l \le 14$
2θ max	90.72°	91.28°	90.72°
Measured reflections	27170	22951	14278
Unique reflections	8678	5483	5504
Reflections used	6358	4315	3988
Max/min transmission	0.7489/0.6600	0.6367/0.7489	0.6574/0.7489
Number of parameters	214	142	142
Max/min electron density	4.368/-3.341	4.105/-2.435	4.442/-2.729
Goodness-of-fit on $\|F^2\|$	0.964	1.060	0.970
R indices	R_1 (>4σ) = 0.0300 wR_2 = 0.0538 R_1 (all data) = 0.0566	R_1 (>4σ) = 0.0456 wR_2 = 0.0893 R_1 (all data) = 0.0685	R_1 (>4σ) = 0.0397 wR_2 = 0.1010 R_1 (all data) = 0.0691

Table 2. Comparison of the refinement results for the $RE_2Mo_9O_{19}$ crystals for models placing Mo3 atoms on either the 1*f* or 2*i* sites.

Phase	Site	Site location	U_{22}	U_{33}	U_{eq}	R_1 value
$La_2Mo_9O_{19}$	1*f*	x = 0.5 y = 0 z = 0.5	0.0252(4)	0.0096(3)	0.0212(2)	0.0543
	2*i*	x = 0.5013(2) y = 0.0191(2) z = 0.5103(2)	0.0037(4)	0.0039(3)	0.0034(1)	0.0456
$Ce_2Mo_9O_{19}$	1*f*	x = 0.5 y = 0 z = 0.5	0.0231(4)	0.0094(2)	0.0206(2)	0.0483
	2*i*	x = 0.5023(2) y = 0.0186(2) z = 0.5104(2)	0.0032(4)	0.0035(3)	0.0034(1)	0.0397

Table 3. Experimentally determined magnetic and electrical properties of $RE_3Mo_{14}O_{30}$ and $RE_2Mo_9O_{19}$ samples.

Sample	**χ_0 (emu/mol)**	**Θ (K)**	**μ_{eff} /f.u. (μ_B)**	**μ_{eff} /Mo (μ_B)**	**μ_{eff} /*RE* (μ_B)**	**ρ at 298 K (Ohm cm)**	**Activation Energy (eV)**
$La_3Mo_{14}O_{30}$	$1x10^{-3}$	-33	2.1	0.6	-	32.8	0.125
$La_2Mo_9O_{19}$	$3x10^{-5}$	-8	0.6	0.2	-	333	0.117
$Ce_2Mo_9O_{19}$	$7x10^{-4}$	-20	3.3	0.2[a]	2.3	1220	0.146

[a] Assumed based on the results obtained from the $La_2Mo_9O_{19}$ sample.

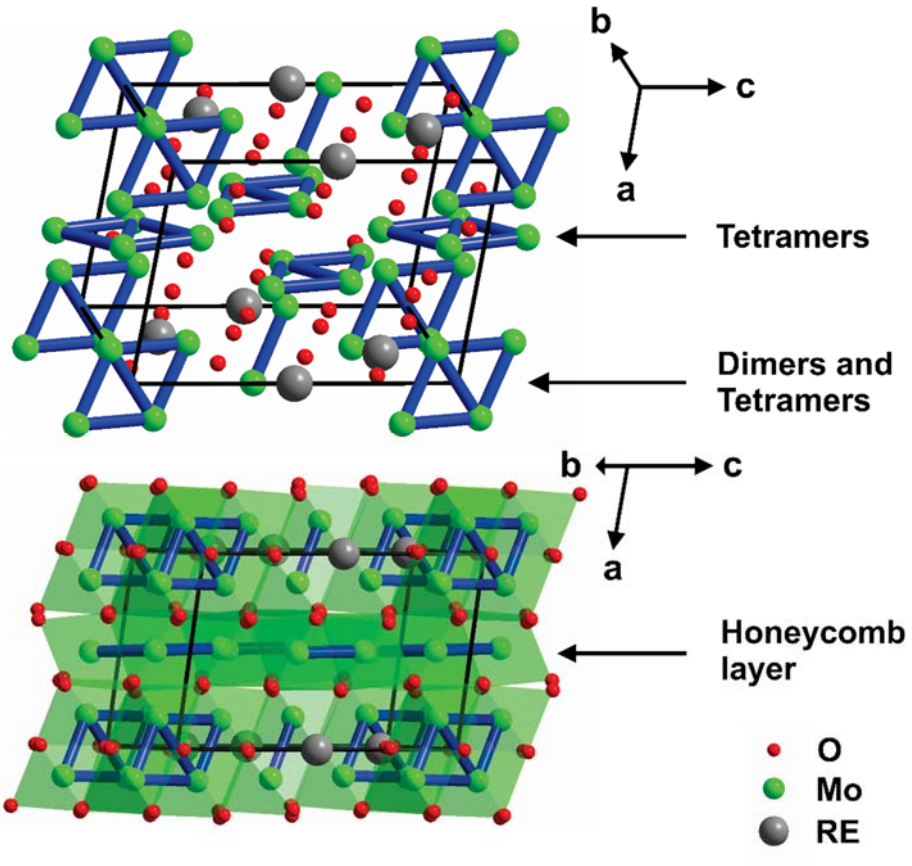

Figure 1. The $RE_3Mo_{14}O_{30}$ structure viewed along different directions of its unit cell. MoO_6 octahedra (green) form the overall framework of the structure. The resulting spatial arrangement of MoO_6 octahedra gives rise to Mo-Mo bonds (blue).

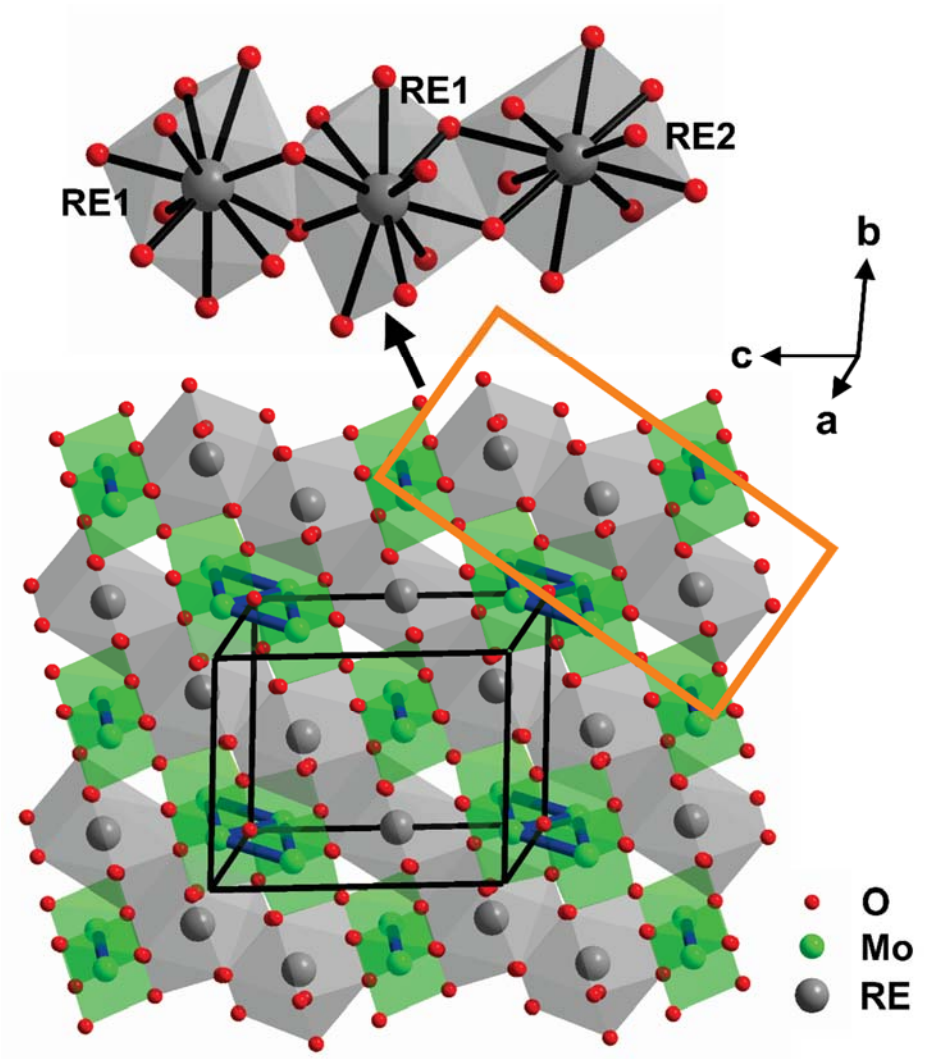

Figure 2. The *RE*-O layer of the $RE_3Mo_{14}O_{30}$ structure. RE_3O_{26} polyhedral units (gray) form an infinite chain within the structure. These chains are separated by concurrent chains of MoO_6 octahedra (green).

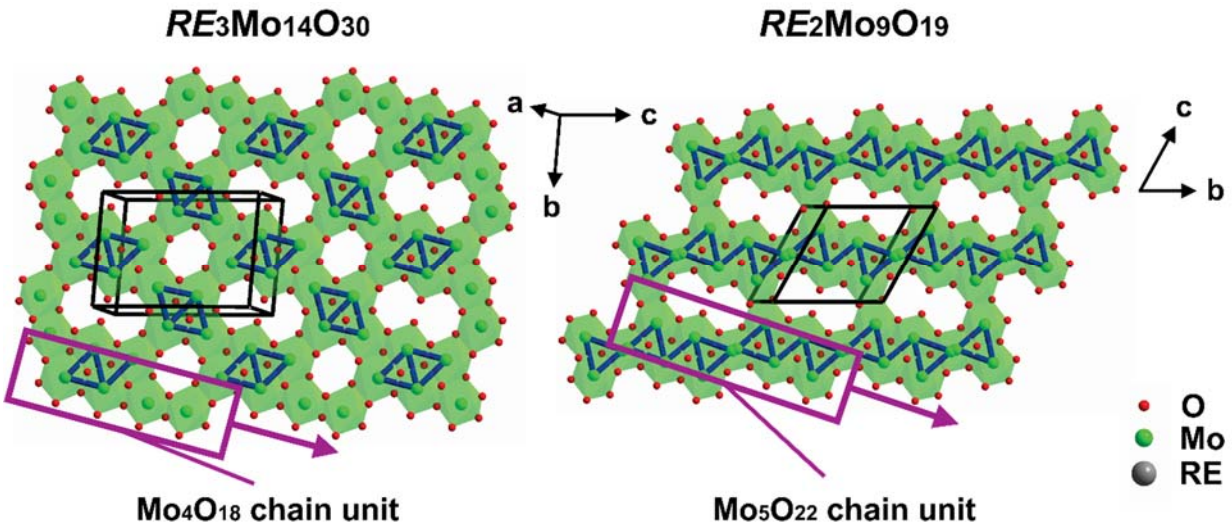

Figure 3. Defect honeycomb layers of $RE_3Mo_{14}O_{30}$ (left) and $RE_2Mo_9O_{19}$ (right). The arrangement of MoO_6 octahedra in each structure gives rise to different arrangements of Mo-Mo bonding interactions (blue). The different MoO_6 octahedral chain units are highlighted in each structure (purple).

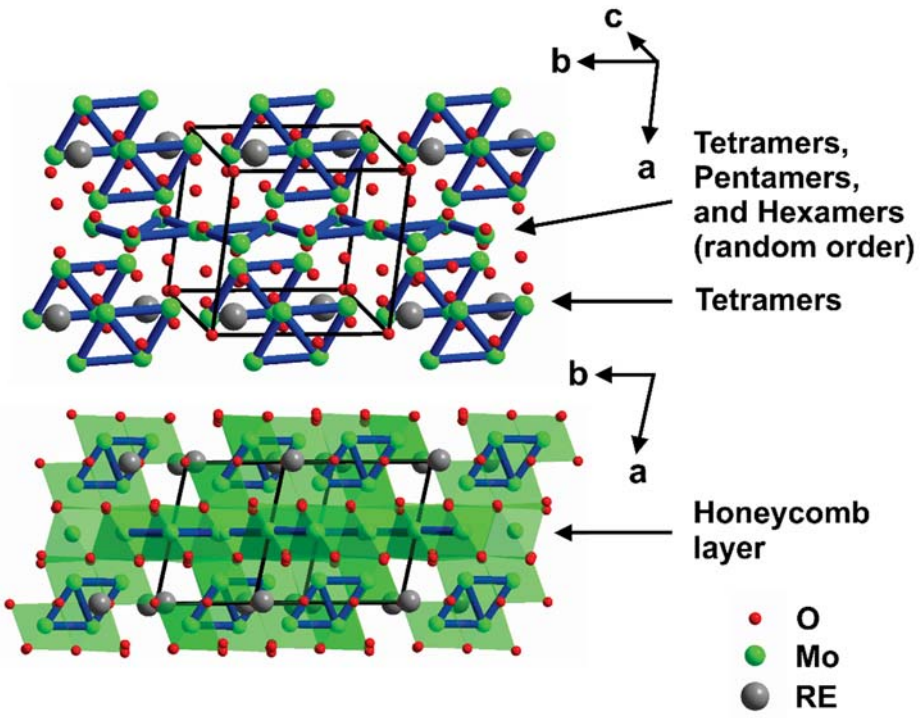

Figure 4. The $RE_2Mo_9O_{19}$ structure viewed along different directions of its unit cell. MoO_6 octahedra (green) form the overall framework of the structure. The resulting spatial arrangement of MoO_6 octahedra gives rise to Mo-Mo bonds (blue).

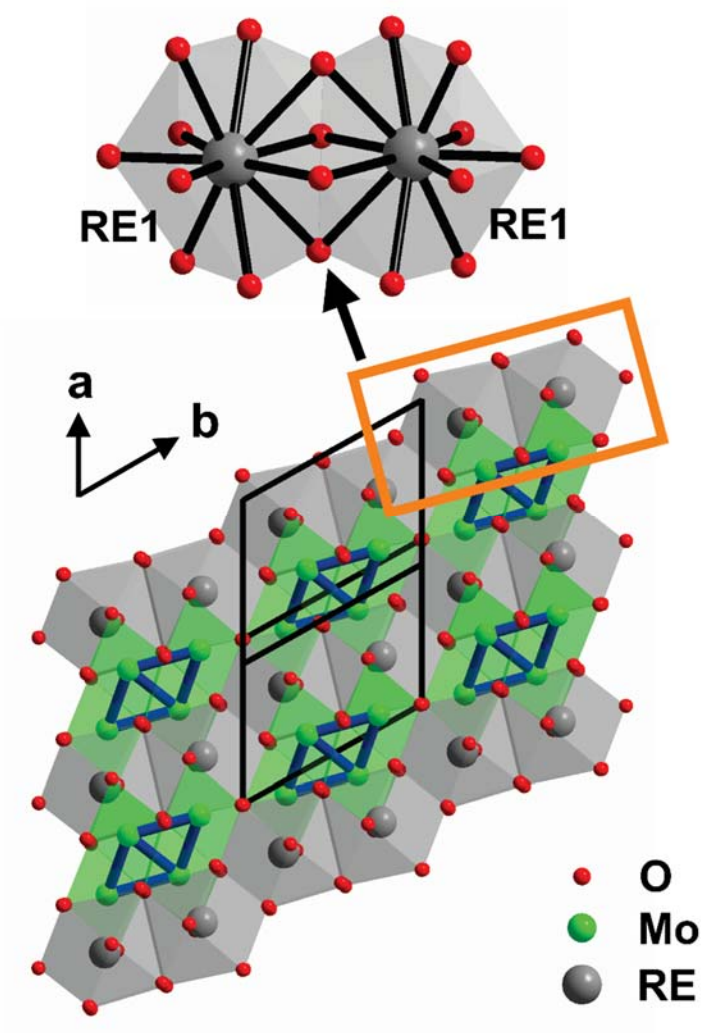

Figure 5. The *RE*-O layer of the $RE_2Mo_9O_{19}$ structure. RE_2O_{18} polyhedral units (gray) form an infinite chain within the structure. These chains are separated by concurrent chains of MoO_6 octahedra (green).

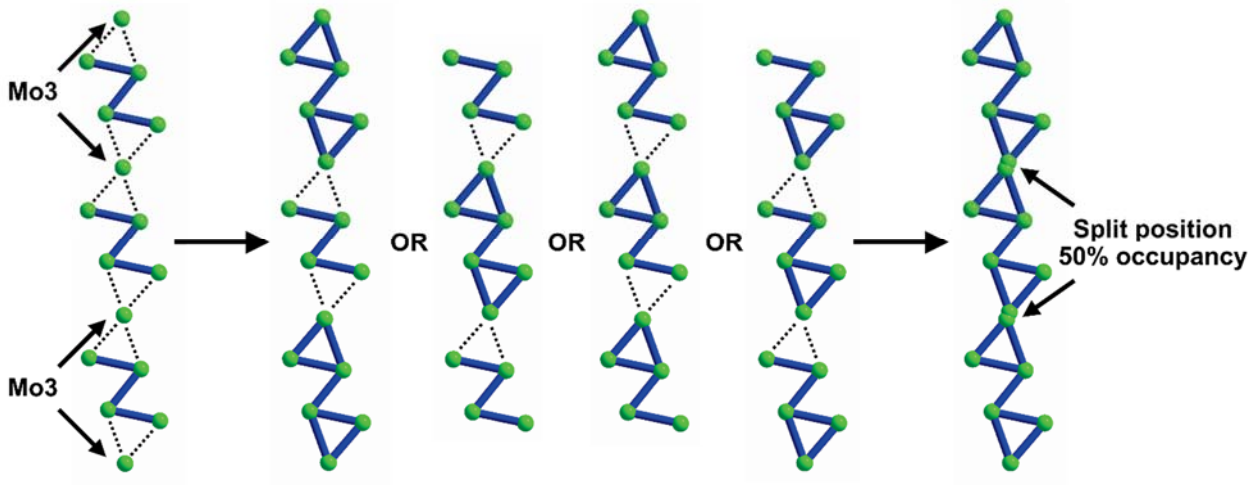

Figure 6. Formation of random arrangements of Mo tetramers, pentamers, and hexamers (blue) as a result of disorder of Mo3 atoms in $RE_2Mo_9O_{19}$. Non-bonding interactions are represented by dashed lines. The default crystal solution assumes Mo3 atoms to occupy a 1*f* site, although high temperature factors are observed (left). The resulting delocalization (middle) yields a better solution and allows for the formation of a random sequence of tetramers, pentamers, and hexamers (right).

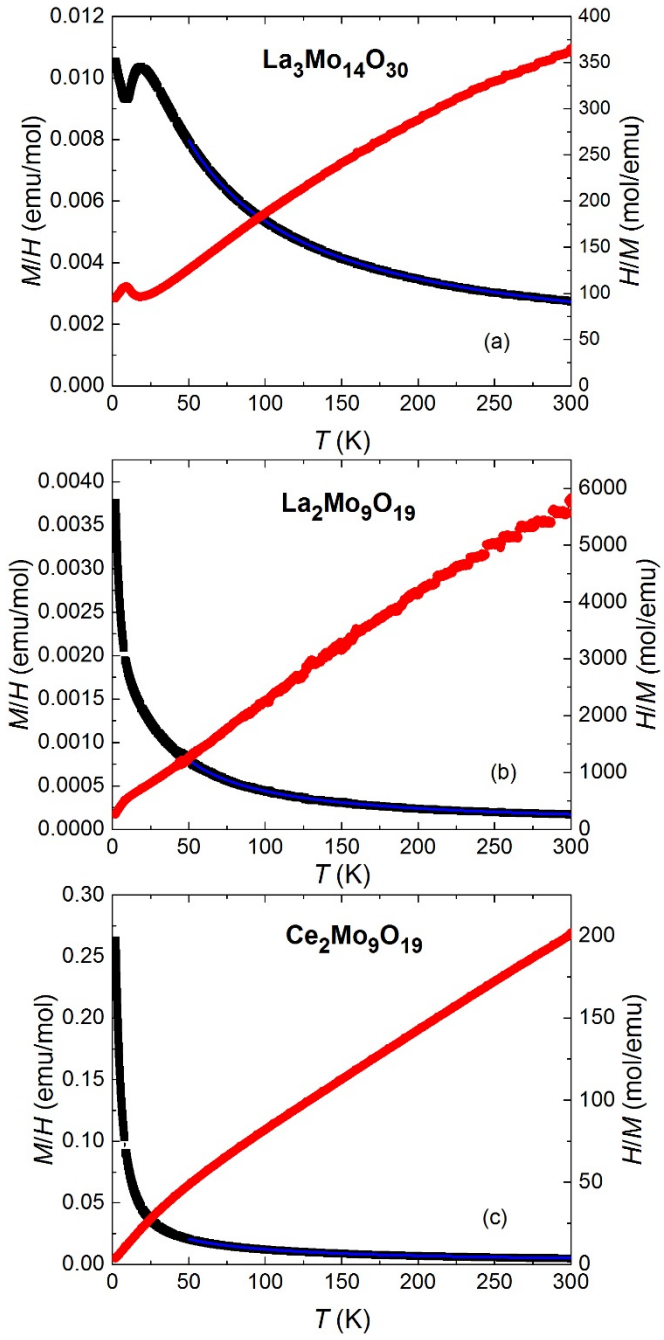

Figure 7. Effective magnetic moment vs temperature for $La_3Mo_{14}O_{30}$ (top), $La_2Mo_9O_{19}$ (middle), and $Ce_2Mo_9O_{19}$ (bottom). The magnetic moment data (black) and the inverse susceptibility data (red) are both displayed. The Curie-Weiss fit for each magnetic moment data set (thin blue line) is also displayed.

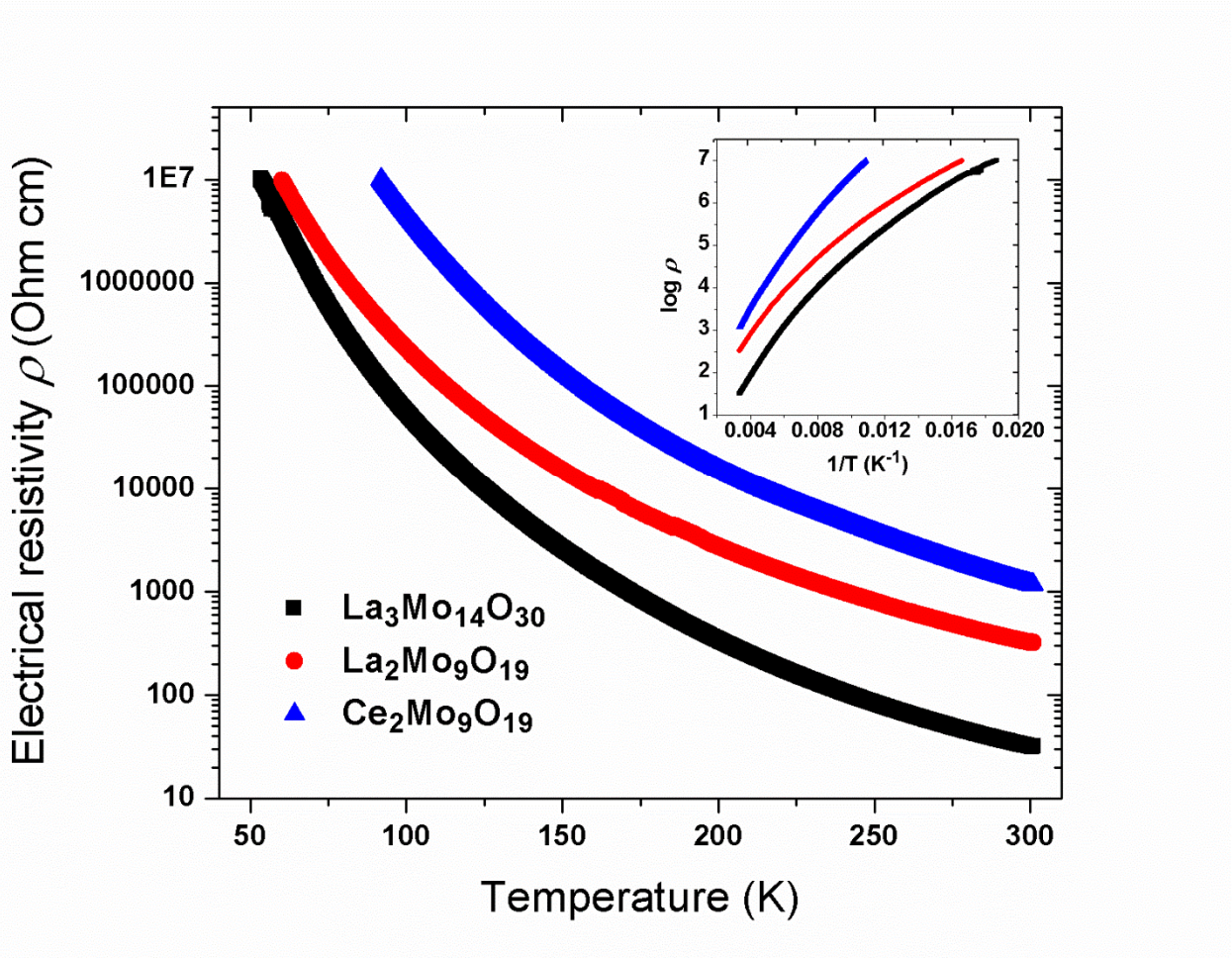

Figure 8. Electrical resistivities of the phase pure $RE_3Mo_{14}O_{30}$ and $RE_2Mo_9O_{19}$ samples.

References

(1) Fischer, O. Chevrel Phases: Superconducting and Normal State Properties. *Appl. Phys.* **1978**, *16* (1), 1–28.

(2) Gougeon, P.; Potel, M.; Gautier, R. Syntheses and Structural, Physical, and Theoretical Studies of the Novel Isostructural Mo_9 Cluster Compounds $Ag_{(2.6)}CsMo_9Se_{11}$, $Ag_{(4.1)}ClMo_9Se_{11}$, and H-Mo_9Se_{11} with Tunnel Structures. *Inorg. Chem.* **2004**, *43* (4), 1257–1263.

(3) Gougeon, P.; Potel, M.; Padiou, J.; Sergent, M. Silver Molybdenum Telluride ($AgMo_6Te_6$): A New One-Dimensional Structure Type Having Linear Chains $|Mo_{6/2}|_{\infty 1}$. *J. Solid State Chem.* **1987**, *68* (1), 137–142.

(4) Chevrel, R.; Gougeon, P.; Potel, M.; Sergent, M. Ternary Molybdenum Chalcogenides: A Route to New Extended Clusters. *J. Solid State Chem.* **1985**, *57* (1), 25–33.

(5) Fischer, O.; Maple, M. B.; Editors. *Topics in Current Physics, Vol. 32: Superconductivity in Ternary Compounds I: Structural, Electronic, and Lattice Properties.*; Springer-Verlag, **1982**.

(6) Matthias, B. T.; Marezio, M.; Corenzwit, E.; Cooper, A. S.; Barz, H. E. High-Temperature Superconductors, the First Ternary System. *Science* **1972**, *175* (4029), 1465–1466.

(7) Leligny, H.; Labbe, P.; Ledesert, M.; Hervieu, M.; Raveau, B.; McCarroll, W. H. The Modulated Structure of Lanthanum Octamolybdate. *Acta Crystallogr. Sect. B Struct. Sci.* **1993**, *B49* (3), 444–454.

(8) Gall, P.; Gougeon, P. Structure of Lanthanum Molybdenum Oxide ($La_4Mo_2O_{11}$) Containing Isolated Mo_2O_{10} Cluster Units. *Acta Crystallogr. Sect. C Cryst. Struct. Commun.* **1992**, *C48* (11), 1915–1917.

(9) Torardi, C. C.; McCarley, R. E. Sodium Tetramolybdenum Hexoxide ($NaMo_4O_6$). A Metallic Infinite-Chain Polymer Derived by Condensation of Octahedral Clusters. *J. Am. Chem. Soc.* **1979**, *101* (14), 3963–3964.

(10) Tortelier, J.; Gougeon, P.; Gautier, R.; Berjoan, R. $MTi_{0.7}Mo_{0.3}Mo_5O_{10}$ (M = Sr, Eu), First Evidence of Mono- and Bicapped Bioctahedral Mo_{11} and Mo_{12} Clusters: Synthesis, Crystal Structures, and Physical Properties. *Inorg. Chem.* **2001**, *40* (10), 2292–2297.

(11) Tortelier, J.; Gougeon, P.; Ramanujachary, K. V; Greenblatt, M. Synthesis and Physical Properties of $M_4M'_3Mo_{26}O_{48}$ (M = Sr, Eu; M' = Al, Ga) Containing Mo_7 Clusters and Infinite Mo_7-Mo_{10}-Mo_7 Chains. *Mater. Res. Bull.* **1998**, *33* (8), 1151–1157.

(12) Tortelier, J.; Gougeon, P. $Pr_4Mo_9O_{18}$, an Atypical, Novel, Ternary Reduced Molybdenum Oxide Containing Unusual Mo_7, Mo_{13}, and Mo_{19} Clusters. Synthesis, Crystal Structure, and Physical Properties. *Inorg. Chem.* **1998**, *37* (24), 6229–6236.

(13) Balandin, A. A.; Ghosh, S.; Bao, W.; Calizo, I.; Teweldebrhan, D.; Miao, F.; Lau, C. N. Superior Thermal Conductivity of Single-Layer Graphene. *Nano Lett.* **2008**, *8* (3), 902–907.

(14) Stankovich, S.; Dikin, D. A.; Dommett, G. H. B.; Kohlhaas, K. M.; Zimney, E. J.; Stach, E. A.; Piner, R. D.; Nguyen, S. T.; Ruoff, R. S. Graphene-Based Composite Materials. *Nat. (London, United Kingdom)* **2006**, *442* (7100), 282–286.

(15) Zhang, Y.; Tan, Y.-W.; Stormer, H. L.; Kim, P. Experimental Observation of the Quantum Hall Effect and Berry's Phase in Graphene. *Nat. (London, United Kingdom)* **2005**, *438* (7065), 201–204.

(16) Banerjee, A.; Bridges, C. A.; Yan, J.-Q.; Aczel, A. A.; Li, L.; Stone, M. B.; Granroth, G. E.; Lumsden, M. D.; Yiu, Y.; Knolle, J.; Bhattacharjee, S.; Kovrizhin, D. L.; Moessner,

R.; Tennant, D. A.; Mandrus, D. G.; Nagler, S. E. Proximate Kitaev Quantum Spin Liquid Behaviour in a Honeycomb Magnet. *Nat. Mater.* **2016**.
(17) Jain, S. C.; Willander, M.; Narayan, J.; Van Overstraeten, R. III-Nitrides: Growth, Characterization, and Properties. *J. Appl. Phys.* **2000**, *87* (3), 965–1006.
(18) Strite, S.; Morkoc, H. Gallium Nitride, Aluminum Nitride and Indium Nitride: A Review. *J. Vac. Sci. Technol. B Microelectron. Nanom. Struct.* **1992**, *10* (4), 1237–1266.
(19) Regnault, L. P.; Rossat-Mignod, J.; Henry, J. Y.; de Jongh, L. J. Magnetic Properties of the Quasi-2d Easy Plane Antiferromagnet $BaNi_2(PO_4)_2$. *J. Magn. Magn. Mater.* **1983**, *31* (Part 3), 1205–1206.
(20) He, Z.; Ueda, Y. Magnetic Properties of $Mn_2V_2O_7$ Single Crystals. *J. Solid State Chem.* **2008**, *181* (2), 235–238.
(21) Sharma, N. L.; Tanaka, T. Superionic Conduction in the Solid-Solution Electrode Silver Chromium Sulfide ($AgCrS_2$). *Phys. Rev. B Condens. Matter Mater. Phys.* **1983**, *28* (4), 2146–2151.
(22) Kimber, S. A. J.; Ling, C. D.; Morris, D. J. P.; Chemseddine, A.; Henry, P. F.; Argyriou, D. N. Interlayer Tuning of Electronic and Magnetic Properties in Honeycomb Ordered $Ag_3LiRu_2O_6$. *J. Mater. Chem.* **2010**, *20* (37), 8021–8025.
(23) Miura, Y.; Yasui, Y.; Sato, M.; Igawa, N.; Kakurai, K. New-Type Phase Transition of Li_2RuO_3 with Honeycomb Structure. *J. Phys. Soc. Japan* **2007**, *76* (3), 033705/1-033705/4.
(24) Zhang, H.-J.; Chadov, S.; Muchler, L.; Yan, B.; Qi, X.-L.; Kubler, J.; Zhang, S.-C.; Felser, C. Topological Insulators in Ternary Compounds with a Honeycomb Lattice. *Phys. Rev. Lett.* **2011**, *106* (15), 156402/1-156402/4.
(25) Shamoto, S.; Kato, T.; Ono, Y.; Miyazaki, Y.; Ohoyama, K.; Ohashi, M.; Yamaguchi, Y.; Kajitani, T. Structures of β-ZrNCl and Superconducting $Li_{0.16}ZrNCl$: Double Honeycomb Lattice Superconductor. *Phys. C Supercond.* **1998**, *306* (1&2), 7–14.
(26) Bruker Analytical X-Ray Systems. Madison, WI, USA **2002**.
(27) Sheldrick, G. M. SHELXL. University of Gottingen, Germany **1997**.
(28) Hunter, B. A. H.; Howard, C. J. Rietica - a Visual Rietveld Program. In *Rietica Australian Nuclear Science and Technology Organization: Menai, Australia*; Australia, **2000**.
(29) Shannon, R. D. Revised Effective Ionic Radii and Systematic Studies of Interatomic Distances in Halides and Chalcogenides. *Acta Crystallogr. Sect. A Cryst. Physics, Diffraction, Theor. Gen. Crystallogr.* **1976**, *A32* (5), 751–767.
(30) Brese, N. E.; O'Keeffe, M. Bond-Valence Parameters for Solids. *Acta Crystallogr. Sect. B Struct. Sci.* **1991**, *B47* (2), 192–197.
(31) Toriyama, T.; Watanabe, M.; Konishi, T.; Ohta, Y. Superatomic Crystal Emerging in Transition-Metal Oxides: Molybdenum Hollandite $K_2Mo_8O_{16}$. *Phys. Rev. B* **2013**, *88* (23), 235116.
(32) Torardi, C. C.; McCarley, R. E. Synthesis, Crystal Structures, and Properties of Lithium Zinc Molybdenum Oxide ($LiZn_2Mo_3O_8$), Zinc Molybdenum Oxide ($Zn_3Mo_3O_8$), and Scandium Zinc Molybdenum Oxide ($ScZnMo_3O_8$), Reduced Derivatives Containing the Mo_3O_{13} Cluster Unit. *Inorg. Chem.* **1985**, *24* (4), 476–481.
(33) Wang, Y.; Zhou, Z.; Wen, T.; Zhou, Y.; Li, N.; Han, F.; Xiao, Y.; Chow, P.; Sun, J.; Pravica, M.; Cornelius, A. L.; Yang, W.; Zhao, Y. Pressure-Driven Cooperative Spin-Crossover, Large-Volume Collapse, and Semiconductor-to-Metal Transition in Manganese(II) Honeycomb Lattices. *J. Am. Chem. Soc.* **2016**, *138* (48), 15751–15757.

(34) Brown, I. D.; Wu, K. K. Empirical Parameters for Calculating Cation-Oxygen Bond Valences. *Acta Crystallogr. Sect. B Struct. Crystallogr. Cryst. Chem.* **1976**, *B32* (7), 1957–1959.
(35) Hamilton, W. C. Significance Tests on the Crystallographic R Factor. *Acta Crystallogr.* **1965**, *18* (3), 502–510.
(36) Tortelier, J.; Mccarroll, W. H.; Gougeon, P. Synthesis, Crystal Structure, and Characterization of the New Ordered Hollandite-Type $NdMo_6O_{12}$. *J. Solid State Chem.* **1998**, *136* (1), 87–92.
(37) Lofland, S. E.; Scabarozi, T.; Ramanujachary, K. V; McCarroll, W. H. Unusual Magnetic Properties of $La_5Mo_4O_{16}$. *J. Magn. Magn. Mater.* **2003**, *260* (1–2), 184–187.
(38) *CRC Handbook of Chemistry and Physics*, 92nd ed.; Haynes, W. M., Ed.; CRC Press: Boca Raton, FL, **2016**.
(39) Schlottmann, P. Effects of Spin-Orbit Splitting on the Ground State of a Cerium Ion. *J. Phys. C Solid State Phys.* **1985**, *18* (9), 1865–1872.

Table of Contents Graphic